nature communications

Article

https://doi.org/10.1038/s41467-025-57528-9

Dissipative charge transport in organic mixed ionic-electronic conductor channels

Received: 2 December 2024

Accepted: 24 February 2025

Published online: 13 March 2025

Check for updates

Filippo Bonafè[1,2], Mattia Bazzani[1,2], Beatrice Fraboni[1] & Tobias Cramer[1]

Understanding charge transport in organic mixed ionic-electronic conductors (OMIECs) is crucial to improve the performances of bioelectronic and neuromorphic devices. Recent studies reveal that the amplification of electrical signals in organic electrochemical transistors is determined by the volumetric capacitance c_v and electronic mobility μ_e of OMIEC channels, but how material parameters impact on the signal propagation speed and energy dissipation remains unclear. To address this issue, we combine electrical measurements of the phase velocity in microstructured OMIEC channels with local measurements of ionic displacements with modulated electrochemical atomic force microscopy. We interpret experimental data with a simplified transmission line model to determine the dispersion relation for OMIEC channels. We demonstrate that at relevant frequencies the phase velocity is dominated by the ratio of μ_{el}/c_v, constituting an additional figure of merit to benchmark material formulations. These results highlight intrinsic limitations of OMIEC-based circuits and compare their efficiency with neuronal signal transmission.

Highly efficient bioelectronic interfaces designed to sense or trigger biological processes require transducing materials that can effectively convert ionic fluxes in an aqueous environment into electrical signals[1]. Organic mixed ionic-electronic conductors (OMIECs) have recently gained significant attention in this field of research due to their ability to conduct ions in addition to electrons and holes[2] combined with material biocompatibility, soft mechanical properties, and facile processing[3]. OMIEC formulations are currently explored for a variety of applications, ranging from microelectrode arrays for in vitro[4] and in vivo[5] bioelectronics, organic electrochemical transistors[6], and neuromorphic circuits[7] to ultra-conformable wearable electronics[8] and artificial tissues[9] based on conductive hydrogels. In all these applications, the transmission of signals through the bioelectronic circuit is required to happen on fast timescales and with small dissipation of energy in the form of joule heating. For single carrier conductors, simple answers to these questions are provided by standard electrical circuit theory[10]. Bioelectronic electrodes are ultimately specialized conductive cables designed to propagate electromagnetic waves. Transmission line theory can be used to calculate the voltage and current distributions given the distributed resistance, inductance and capacitance of the cable[11], while Joule's equation can be applied to determine the amount of energy dissipated as heat. For mixed conducting channels in contact with an electrolyte bath, the situation is more complex. Signal transduction is always related to carrier transport, but such process in OMIECs involves charge carriers with different nature which interact in the entire material bulk[12]. Ionic and electronic transport in OMIEC channels occurs along different directions in multiple material phases and operates on distinct timescales[13]. To optimize novel materials and to design circuits and assess their dissipation, it is fundamental to understand how transport in such mixed conductor channels depends on material properties and on the geometry of conducting channels. Furthermore, it is interesting to compare the performance of typical bioelectronic devices in terms of efficiency and velocity of signal transmission to neurons, which constitute naturally-evolved systems for bioelectronic signal propagation[14].

The modeling of transport in OMIECs has advanced significantly in recent years. Generally accepted approaches describe the bulk transport with drift diffusion models[15] aiming to reproduce the experimental characteristics of OMIEC applications such as electrolyte-coupled electrodes[16,17] or organic electrochemical transistors[18,19]. In these studies the OMIEC bulk is discretized into finite

[1]Department of Physics and Astronomy, University of Bologna, Viale Berti Pichat 6/2, 40127 Bologna, Italy. [2]These authors contributed equally: Filippo Bonafè, Mattia Bazzani. e-mail: tobias.cramer@unibo.it

volume elements, and the Poisson and continuity equations are solved in a self-consistent scheme to determine the local distribution of ionic and electronic carriers and electrical potential[18]. In mixed conductors the volume element is described by the electronic and ionic resistivity ρ_{el} and ρ_{ion} and the capacitance c_v describing how changes in the chemical potential impact on the accumulation of ionic and electronic carriers. Different physical processes contribute to the capacitance and are described in literature with differing terminology. The chemical capacitance describes how changes in the local distribution of ionic and electronic carrier numbers impact on the entropy of the volume cell and affect its free energy[20]. The quantum capacitance depends on the density of states of the semiconductor describing the energetics of electronic carrier accumulation[21]. Finally, experimental findings demonstrate a nanophase separated structure of OMIECs in which electronic and ionic carriers are expected to reside in spatially separated ionic and electronic phases (see Fig. 1)[22]. Accordingly, also an electrostatic interaction contributes to the free energy needed to accumulate local carriers (electrostatic capacitance). Each of these three contributions scales with the size of the volume element, and it is thus possible to introduce the volumetric capacitance c_v without further distinguishing the microscopic origin. Typical experimental values found for c_v in OMIECs are on the order of $c_v > 30$ F cm^{-3}[23].

Figure 1 visualizes a finite volume element for the modeling of OMIEC materials and devices. For the case of an OMIEC channel immersed in an electrolyte bath, two different dimensions for transport must be considered. Transport along the device channel is usually associated to the horizontal direction that spans from $0 \le x \le L$. Transport in the orthogonal y-direction occurs along the thickness t_h of the thin film channel. For each of these directions ionic and electronic currents must be considered and are described by a total of four carrier paths. For the bulk of the OMIEC, one can assume charge neutrality of the volume element and the sum of all incoming and outgoing ionic or electronic currents must be balanced. As Kirchhoff's laws are valid one can demonstrate that a material consisting of mixed conductor volume elements can be represented for small signal analysis by an exact equivalent circuit model directly derived from the drift-diffusion equations[24]. This was exploited for one dimensional experiments to understand for example the impedance analysis of conducting polymer electrodes[25], the swelling dynamics in OMIEC electroactuators[26], or transient regimes in electrolyte-gated transistors[19].

In this work, we extend the equivalent circuit analysis, and we account for transport in different spatial directions and multiple frequencies as relevant for transport along OMIEC channels in contact with an electrolyte bath. We show how the equivalent circuit simplifies into a transmission line model and how analytical solutions can be derived to describe the velocity and dissipation of signals through mixed conductors. We verify our model with experimental findings on electrical signal propagation in microstructured PEDOT:PSS channels of different length at different frequencies. We compare data obtained from direct electrical measurements with local measurements of ionic displacements done with modulated electrochemical atomic force microscopy. By combining the experimental data with the transmission line model, we resolve the dispersion relation for transport in OMIECs, demonstrating how fundamental material parameters determine the velocity of signal transmission through mixed conductors and the related energy dissipation. The signal propagation efficiency of OMIEC materials is finally compared with transport along the axon in biological neurons to identify some principal limits in OMIECs based circuits.

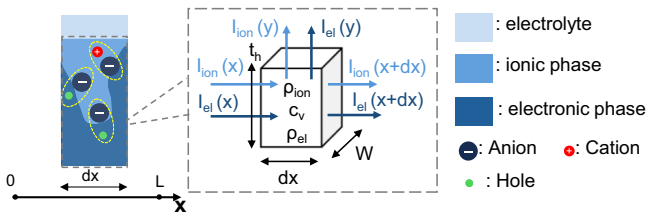

Fig. 1 | Modeling OMIEC thin films containing nanoscale interfaces between ionic and electronic conducting phases. An infinitesimal volume element with length dx, width W and thickness t_h represents bulk transport in the film. Ionic and electronic charge carriers accumulate at the internal interfaces of the volume element described by a volumetric capacitance c_v. Electronic and ionic currents (I_{el}, I_{on}) must be considered in the direction along the thin film (x) and in the orthogonal direction (y). Transport properties are described by ionic and electronic resistivities ρ_{ion} and ρ_{el}.

Results

Modelling charge transport in systems with dissipative electrical signal propagation

In our work we are interested in the propagation of an electrical signal through an OMIEC channel immersed in an electrolyte as illustrated in Fig. 2. A voltage V (measured vs an Ag/AgCl electrode) is injected into a PEDOT:PSS thin film at time $t = 0$ and position $x = 0$ and then travels through the mixed-conducting layer with length L, width W and thickness t_h. The moving potential front alters the local charge distribution through the ejection of mobile cations which electrostatically couple with fixed PSS^- acceptors in the ionic phase of the material generating an outflux of cations to keep electroneutrality. Consequently, a fraction of the electronic current traveling along the channel is dissipated through capacitive ionic currents flowing from the OMIEC layer into the surrounding electrolyte.

Based on the model for the volume element of a mixed conductor as introduced in Fig.1, we derive the equivalent circuit describing the signal propagation shown in Fig. 2a. In the horizontal direction, we simplify the circuit by considering only the electronic carrier path described by the electronic resistance per unit length r_O (measured in Ω/m). This is justified by the electronic conductivity of the OMIEC channel exceeding by several orders of magnitude its ionic counterpart[27]. In addition, the gold electrode acts as a selective contact for electronic carriers and sets the boundary condition at $x = 0$ imposing the voltage $V(x = 0,t)$ of the injected signal. At $x = L$ we have the high impedance contact of a voltmeter V_{out} that interrupts the transmission line. In the vertical direction, boundary conditions are determined by the inert substrate and by the electrolyte bath acting as a selective contact for ionic carriers. For thin films we assume that the electronic path in the y-direction is at equipotential, and we neglect its electronic resistances. The electronic path is coupled through the volumetric capacitance to the ionic transport path in the y-direction characterized by the ionic resistance r_{ion} of the volume element. Thereby, the characteristic impedance z_O of the vertical line (measured in Ω*m) can be modeled with an RC series circuit as shown in Fig. 2a leading to the transmission line constants

$$r_0 = \frac{\rho_{el}}{W t_h}; \qquad z_0 = \frac{1}{j\omega c_v W t_h} + \frac{\rho_{ion} t_h}{W} \tag{1}$$

The resistance R_{el} is added to the circuit to describe the resistance of the electrolyte. The propagation of an electrical signal along the transmission line satisfies the cable equation (see Supp. Inf. 1):

$$\frac{d^2 V(x,t)}{dx^2} = \gamma^2 V(x,t) \tag{2}$$

where γ is the propagation constant defined as

$$\gamma = \sqrt{\frac{r_0}{z_0}} = \sqrt{\frac{j\omega c_v \rho_{el}}{1 + j\omega c_v \rho_{ion} t_h{}^2}} \tag{3}$$

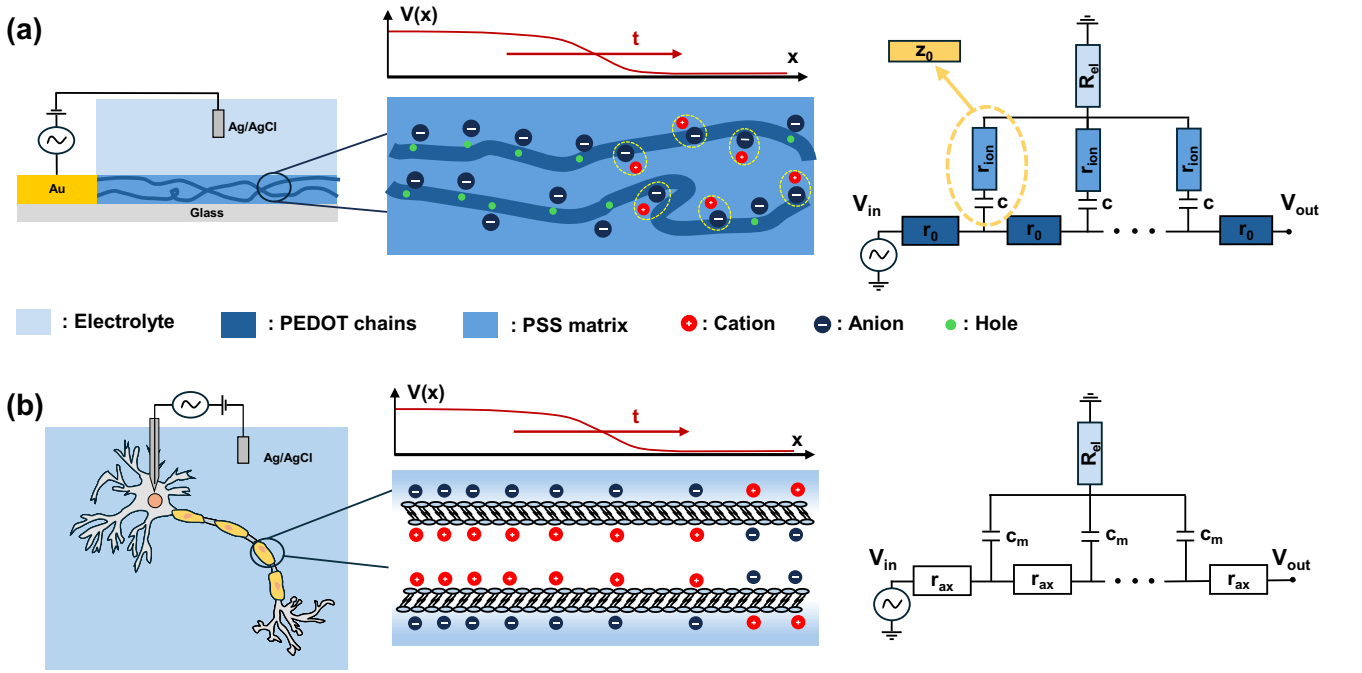

Fig. 2 | Systems with dissipative electrical signal propagation described by transmission line models. a OMIEC channel immersed in an electrolyte. **b** Neural axon surrounded by a physiological medium. For both cases, schematic drawings show the changes in charge distribution during the propagation of an electrical signal V(x,t). In an OMIEC layer the mechanism relies on the coupling between the electronic charge carriers of the conjugated polymer and ions in the polyelectrolyte matrix. Instead for an axon, the ions located in the inner part of the cell membrane are capacitively coupled with the surrounding ionic conductive medium. Despite these differences, both cases are described with similar transmission line models describing how potential waves propagate in the direction parallel to the line while dissipating energy through capacitive currents in the vertical branches of the circuit with the impedances z_0.

As demonstrated by De Levie[28], a solution for Eq. 2 in our set of boundary conditions is

$$V(x,t) = \frac{V_{in}e^{j\omega t}}{1+e^{-2\gamma L}}\left[e^{-\gamma x} + e^{\gamma(x-2L)}\right] \quad (4)$$

where $V_{in}e^{j\omega t}$ is the AC potential applied at $x = 0$ (see Supp. Inf. 2 for the full mathematical treatment). By substituting Eq. 3 in Eq. 4, we obtain a quantitative model that predicts how the propagation of voltage signals along thin OMIEC channels depends on material properties, device geometry, and signal frequency.

The derived transmission line model has a well-known counterpart in biological physics. Nerve pulses traveling along the axon undergo dissipation caused by the coupling with the surrounding biological medium. Mathematical models based on linear cable equations are typically introduced for the specific case of electrical transport along passive neurites where signal propagation does not involve voltage-gated ionic channels[29]. A schematic of the process is reported in Fig. 2b. The propagation of an electrical potential V (measured with respect to a reference electrode placed outside the cell membrane) along the axon modifies the interfacial ionic distribution inside and outside the cell membrane[30]. Ionic charge carriers moving inside the axon are electrostatically coupled with ions located in the surrounding biological medium. Consequently, a fraction of the ionic current traveling along the nerve direction x is dissipated through capacitive currents flowing into the surrounding electrolyte. Such a process can be modeled with the transmission line circuit in Fig. 2b, where r_{ax} (expressed Ω/m) is the ionic resistance per unit length of the interior of the axon, c_m (expressed in F/m) is the membrane capacitance, and R_{el} is the ionic resistance of the cell medium[31]. The description is analogous to the equivalent circuit scheme developed for mixed ionic-electronic conductors. Both naturally-evolved and artificial systems for bioelectronic signal propagation satisfy the same transport equation.

Signal propagation in OMIEC thin films operating at electrolyte interfaces

As a first step for the experimental verification of the transmission line model, we measured the spatiotemporal propagation of an AC potential wave along a micro-structured OMIEC channel. The setup used for this purpose is reported in Fig. 3a and b. A long stripe of a PEDOT:PSS thin film patterned by photolithography ($L = 640$ μm, width $W = 50$ μm, and thickness $t_h = 150 \pm 10$ nm) is contacted by five gold electrodes separated by a distance of 160 μm. The first gold electrode is used to inject the signal $V(x = 0, t) = V_{in}\sin(\omega t) + V_{DC}$ referenced to the electrolyte bath (0.1 M PBS solution with a Ag/AgCl wire as reference electrode). An amplitude V_{in} of 10 mV is applied and the frequency $f = \omega/2\pi$ is swept from 10 Hz to 100 kHz. The constant offset voltage V_{DC} controls the conductivity of PEDOT:PSS through electrochemical doping/de-doping. With the remaining four gold electrodes we measure the local potential $V(x_i,t)$ along the transmission line by connecting the high impedance signal input of a lock-in amplifier. Signals were demodulated to provide the local amplitude and phase shift with respect to the input AC voltage V_{in}. A thick negative photoresist layer (3 μm) was used to electrically insulate the metallic feedlines from the surrounding electrolyte and to minimize parasitic capacitances.

The resulting data showing the propagation of the AC voltage at different sites of the OMIEC channel are reported in Fig. 3b, c. Experimental measurements (indicated with squares) are fitted with theoretical predictions using Eq. 4, where the volumetric capacitance and the electronic and ionic resistivity of PEDOT:PSS (determining the propagation constant γ in Eq. 3) are set as free fitting parameters. The excellent agreement between measurements and the model confirms our initial hypothesis of dissipative charge transport in the OMIEC material. We find that at low frequencies (<10 Hz), the signal shows only minor attenuation along the transmission line and the phase shift is close to 0° (Fig. 3b). With increasing frequencies, the effect of dissipation becomes evident, and the signal amplitude significantly

https://doi.org/10.1038/s41467-025-57528-9

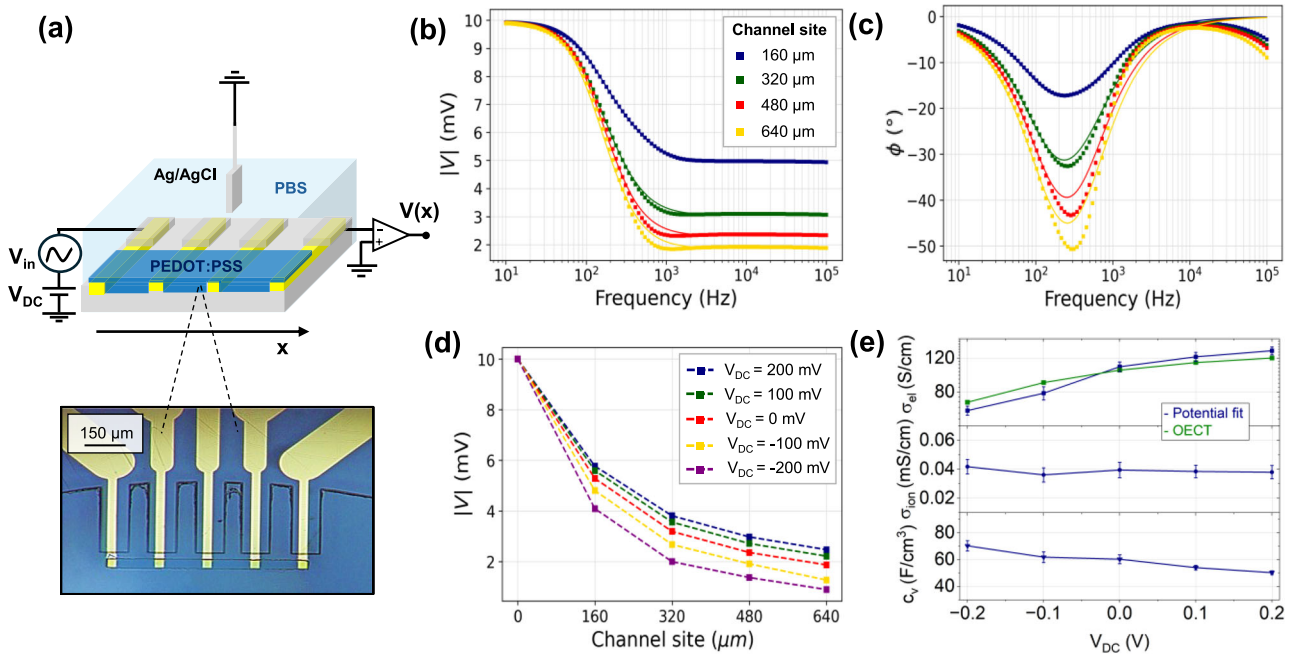

Fig. 3 | Signal propagation in OMIEC thin films operating at electrolyte interfaces. a Schematic representation of the experimental setup featuring an optical micrograph of the experimental samples. Multiple electrodes were designed on the PEDOT:PSS layer to study the propagation of a potential wave at different sites of the OMIEC channel. These are connected to high impedance voltage amplifiers to measure the potential along the channel V(x). A constant offset voltage V_{DC} (applied vs Ag/AgCl to the electrode injecting the AC potential wave) is used to modulate the conductivity of the PEDOT:PSS channel through ion injection. **b** Amplitude and phase (**c**) spectra of potential signals collected at different channel lengths. Experimental data (dots) are fitted with the solution of the cable equation (lines) expressed in Eq. 4 imposing the volumetric capacitance and the ionic and electronic conductivity of the OMIEC layer as free fitting parameters. **d** Signal propagation in an OMIEC thin film at different doping levels. Doping is controlled by applying a DC voltage between the PEDOT:PSS channel and the Ag/AgCl reference electrode. Data collected at a distance $L = 640\,\mu m$ and constant frequency $f = 1\,kHz$ show increased dissipation for lower doping levels. **e** Material parameters extracted from the fits. Error bars indicate the confidence interval of the resulting values. The electronic conductivity of the OMIEC material was also evaluated from organic electrochemical transistor (OECT) characteristics.

decreases while a phase delay gets introduced (Fig. 3c). Data measured at different channel positions demonstrate that signal dissipation is more severe at larger distance from the injecting contact, as the propagating wave travels a longer path through the material. Finally, at higher frequencies (>2 kHz), the signal dissipation becomes independent on frequency and the phase shift goes back to zero. We can interpret the experimental observations with the transmission line model in Fig. 2a. The oscillating electric signal traveling through the channel induces ion movement in and out of the OMIEC film, charging and discharging the volumetric capacitance. For low-frequency signals, the characteristic impedance of the line z_O is large (see Eq. 1) limiting the ionic current flowing into the electrolyte. Thus, the signal propagates with minimal dissipation. As the frequency increases, the capacitive charging in the PEDOT:PSS bulk increases[32], and a stronger displacement current is driven through the OMIEC and the electrolyte, resulting in increased signal amplitude loss and phase shift. This effect is maximized at high frequency, where the dissipated current is fully determined by the ionic resistance of the PSS-rich domains. At that point, the propagated signal amplitude is no longer dependent on frequency, and its phase returns to zero.

Results presented in Fig. 3b and c provide a first experimental proof of the cable equation theory for OMIEC materials. This analysis identifies the propagation constant γ as a fundamental material parameter providing a quantitative metric for the dissipation of traveling signals along the OMIEC channel. As γ is a function of the mixed conductivity and volumetric capacitance of the OMIEC layer (see Eq. 3), we expect that a different channel doping level will result in variations of the dissipation process. The concentration of electronic and ionic carriers in the PEDOT:PSS thin film can be modulated by applying a DC-potential V_{DC} between the sample and the Ag/AgCl reference electrode. In Fig. 3d, V_{DC} is varied between 200 mV and -200 mV inducing the gradual de-doping of the organic semiconductor, while the amplitude of the applied AC voltage V is acquired at a single frequency ($f = 1\,kHz$) on multiple sites along the OMIEC channel. Measurements show that a decrease in the electronic conductivity of the OMIEC material causes stronger dissipation with attenuation of the electrical wave occurring at shorter travelling distances (Fig. 3d). We confirm this finding also with spectroscopic measurements (Suppl. Inf. S3) and we show in Fig. 3e, the resulting fit parameters ρ_{el}, ρ_{ion} and c_v as a function of the applied potential V_{DC}.

The fitting results are consistent with literature findings characterizing PEDOT:PSS mixed transport with optical[33] or electrochemical[34] methods. The PEDOT:PSS volumetric capacitances show slight variations in the potential range of the experiment with values ranging from 50 to 70 F/cm³, in good agreement with previous studies[12]. The electronic conductivity of PEDOT:PSS decreases when negative voltages are applied to the channel, effectively demonstrating the de-doping process associated to increased signal dissipation. Similar values are obtained from organic electrochemical transistor (OECT) DC characteristics (Supp. Inf. 4) confirming the accuracy of our characterization method. In contrast to the electronic conductivity, we find that the ionic conductivity does not change significantly with the PEDOT:PSS doping level. We explain this finding with the large PSS to PEDOT ratio in the PEDOT:PSS formulation used for this experiment[35] leading to a large number of mobile cations compensating the excess PSS^- anions[6,16]. This large quantity of ionic carriers in the PSS-phase determines the ionic conductivity and is only slightly modulated by the ions transferred during the doping process.

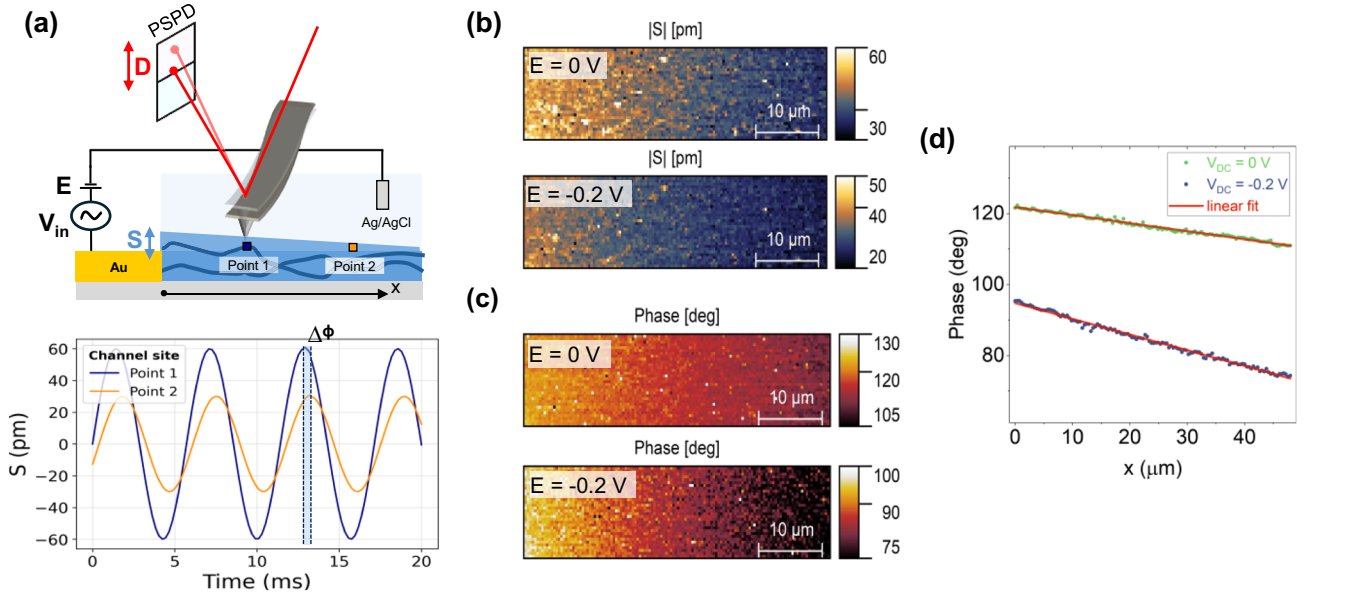

Fig. 4 | Nanoscale measurements of dissipative transport in PEDOT:PSS with modulated-electrochemical atomic force microscopy (mEC-AFM). **a** Experimental setup for mEC-AFM allowing to measure the local electroswelling and strain in PEDOT:PSS induced by the propagating AC potential. Signal traces acquired at frequency f = 1.1 kHz at two different points on the channel surface show the effect of attenuation and dispersion of the voltage wave. Swelling amplitude (**b**) and phase (**c**) mEC-AFM images mapping the local electroactuation of the OMIEC thin film. Measurements are performed at reference doping (E = 0 V) and slightly de-doped channel (E = − 0.2 V). **d** Resulting average phase shift over distance profiles. These were fitted with a linear model to extract the phase velocity quantifying signal transport along the OMIEC channel.

Nanoscale measurements of dissipative transport in OMIEC channels

The electrical measurements discussed so far probe the signal propagation using electrical contacts. Such metallic contacts can alter the boundary conditions for the propagating waves and potentially introduce artifacts. Recently, mEC-AFM measurements were demonstrated to detect local changes in the ionic concentration by measuring the swelling and electrochemical strain in OMIECs[32]. Here we adapt the mEC-AFM method to follow the propagation of the voltage signal along the OMIEC transmission line (see Fig. 4a). An AC potential travelling in an OMIEC channel drives the exchange of ions between the electrolyte and the material bulk. This process causes dynamic volume changes in the channel that propagate as an electrochemical strain wave along with the electrical signal. mEC-AFM experiments can map the amplitude S and phase shift ϕ_S of the strain wave with respect to the injected signal V_{in} by measuring the deflection D of the AFM cantilever induced by the local oscillations of the OMIEC surface. Measurements were performed using NSC36 probes of the Park NX10 AFM on a PEDOT:PSS channel with width $W = 50$ μm and length $L = 1.2$ mm to minimize finite-length effects. The frequency of the applied V_{in} was kept constant at $f = 1.1$ kHz. Swelling oscillations S_1 and S_2 acquired at two different points separated of 50 μm along the horizontal profile of the OMIEC channel x are plotted in Fig. 4a. Because of the attenuation and dispersion of the AC voltage driving the electroswelling process, the signal S_2 measured at a larger distance from the gold electrode (where V_{in} was applied) has smaller amplitude with respect to S_1 and experiences a phase delay. More detailed information can be obtained by acquiring mEC-AFM images providing maps of the local electroactuation amplitude and phase on extended regions of the OMIEC layer. Images with 128 × 32 pixels covering an area of 50 × 12.5 μm of the PEDOT:PSS surface are reported in Fig. 4b, c. Experiments were performed at two different electrochemical potentials to study the effect of the PEDOT:PSS doping level on signal dissipation on a local scale. The acquired data highlight phase and amplitude variations over distance, which become more rapid when PEDOT:PSS is less electronically conductive ($E = -0.2$ V), consistent with macroscopic spectroscopies in Fig. 3.

For a quantitative comparison between the mEC-AFM results and the transmission line theory, we consider the phase shift $\phi(\omega, x)$ measured along the transmission line (Fig. 4d). Following transmission line theory, the phase shift ϕ is directly related to the phase constant $\beta = \mathrm{Im}(\gamma)$ and the phase velocity v_{phase} of the travelling signal wave. For an ideally infinite line (see Supp. Inf. 5 for the complete mathematical treatment), we can write[11]:

$$v_{phase}(\omega) = \frac{\omega}{\beta(\omega)} = -\frac{\omega x}{\phi(\omega, x)} \tag{5}$$

The local phase velocity $v_{phase,loc}$ was calculated from experimental mEC-AFM data from the slope $\beta_{loc} = -\frac{\phi}{x}$ of the linear phase drop resulting by averaging the 32 line-scans in the x direction in Fig. 4c. Results for $E = 0$ V and $E = -0.2$ V are presented in Fig. 4d. $v_{phase,loc}$ values extracted from the fit are compared in Table 1 with values $v_{phase,th}$ calculated using Eq.3 and the material parameters obtained from the spectroscopy experiments (Fig. 3e). More information on this comparison and the explicit analytical expression for dispersion relation $\beta(\omega)$ underlying the phase velocity calculation is provided in Supp. Inf. 5. The excellent agreement between the values in Table 1 demonstrates the intrinsic correlation between the macroscopic dispersion of electrical signals travelling in the OMIEC film and charge transport phenomena occurring at the nanoscale. In parallel, the quantitative agreement between macroscopic spectroscopy experiments and local mEC-AFM measurements proves the absence of electrode-induced artifacts in electrical measurements in Fig. 3, validating our assumptions on boundary conditions for Eq.2. Ionic exchange processes causing the electroswelling of the OMIEC material are responsible for the dissipation of propagating potential waves.

Discussion

Our study shows that the presence of two different transport directions in OMIEC channels – electronic transport parallel to the channel and ionic transport in the orthogonal direction – causes frequency dependent dissipation. The dissipation determines the velocity of

signals travelling along the OMIEC channel and the attenuation of their signal amplitude. Understanding the dissipative processes is crucial to design bioelectronic devices with OMIEC materials. Furthermore, dissipation is directly related to material properties and channel geometry. To illustrate this connection in more detail, we show in Fig. 5a, the phase velocity spectrum for an AC potential wave propagating in a PEDOT:PSS channel with length $L = 640\,\mu m$, width $W = 50\,\mu m$, and thickness $t_h = 150$ nm. Experimental values are obtained applying Eq. 5 to the phase shift data measured in signal propagation spectroscopies (Fig. 3c). Results show a good agreement with transmission line theory predictions calculated from the propagation constant γ of an OMIEC channel (Eq.3 and Supp. Inf. 5).

In addition to the phase delay, propagating signals also experience a decrease in signal amplitude along the channel direction (see Fig. 3b). The process is described by the attenuation coefficient $\alpha = \mathrm{Re}(\gamma)$, which defines the characteristic length scale over which the signal amplitude diminishes. Using our data from signal propagation spectroscopies ($V(x = L, \omega)$, see Supp. Inf. 5) we determine α with

$$\alpha(\omega) = -\frac{1}{L}\ln\left[\frac{|V(x=L,\omega)|}{|V_{in}|}\right] \quad (6)$$

and compare again to predictions calculated from the propagation constant γ of an OMIEC channel (Fig. 5b). In both the attenuation and the phase velocity spectra two different transport regimes can be identified. At lower frequencies, v_{phase} and α increase with the applied frequency which means that faster signals travelling in the OMIEC channels experience a larger attenuation. For the low-frequency regime, a simplified expression for the propagation constant can be derived (see Supp. Inf. 6):

$$\gamma_{LF}(\omega) = \sqrt{\frac{j\omega c_v}{\sigma_{el}}} \quad (7)$$

Experimental data reported in Fig. 5b indicate that the increase rate of the attenuation coefficient with frequency in the low frequency range is slightly smaller than the theoretical limit expressed in Eq. 7. Such discrepancy is possibly caused by finite length effects of the transmission line which complicate the interpretation of the propagation constant γ for the OMIEC channel. As discussed in Supp. Inf. 5, the attenuation coefficient and the phase constant can be calculated as $\alpha = \mathrm{Re}(\gamma)$, $\beta = \mathrm{Im}(\gamma)$ only in the limit of a transmission line with infinite

Table 1 | Comparison between phase velocities measured at f = 1.1 kHz from local mEC-AFM measurements and theoretical values calculated from the propagation constant describing dissipative transport in OMIEC channels

E (V)	$v_{phase,loc}$ (m/s)	$v_{phase,th}$ (m/s)
0	1.82 ± 0.16	1.7 ± 0.3
−0.2	0.90 ± 0.04	0.88 ± 0.12

Material parameters (c_v, ρ_{el}, ρ_{ion}) used for the calculation were obtained from the electrical characterizations reported in Fig. 3

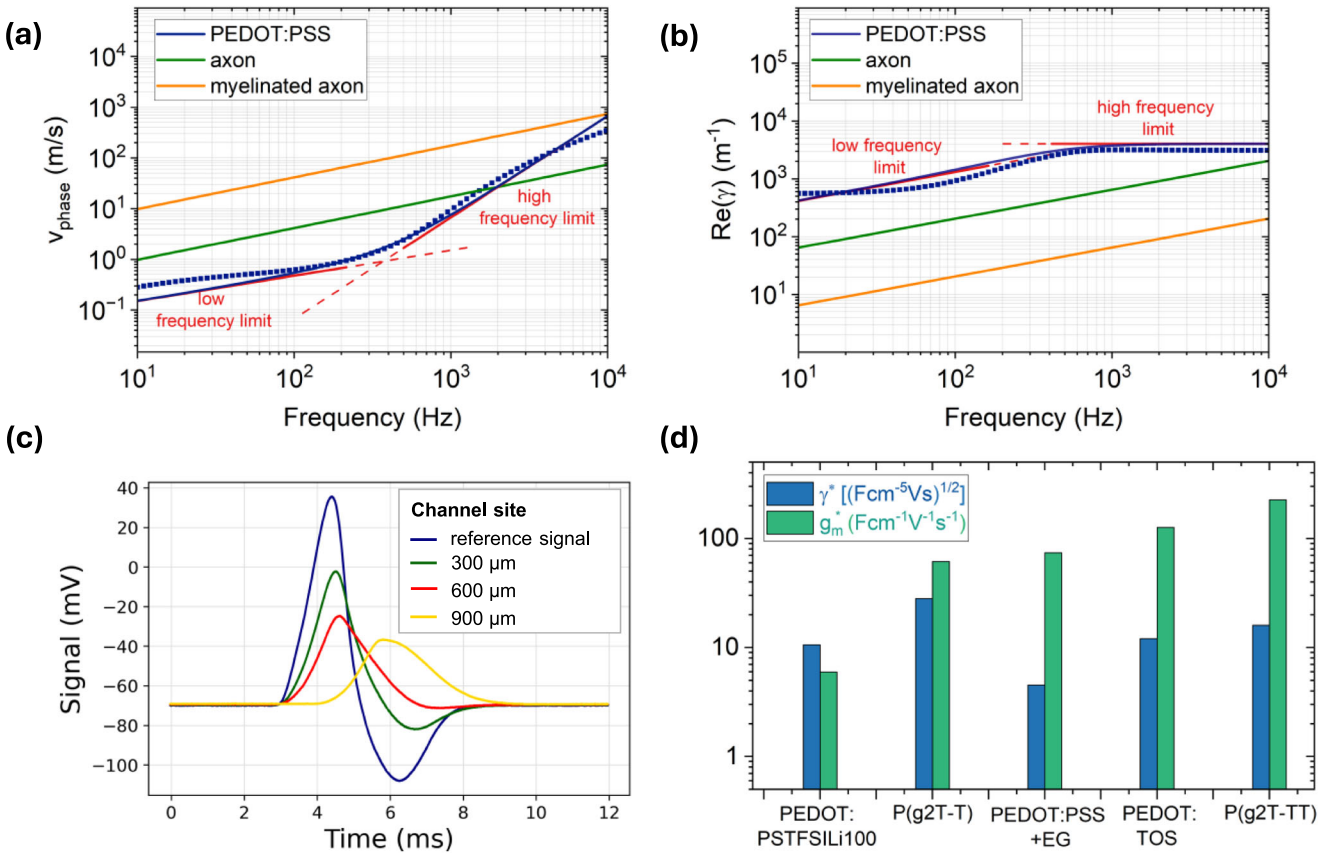

Fig. 5 | Impact of dissipative charge transport on the performances of OMIEC materials. Phase velocity (**a**) and attenuation coefficient (**b**) for a potential wave propagating in a PEDOT:PSS channel. Continuous lines indicate theoretical predictions from the transmission line model, while experimental values resulting from Eq. 5 and Eq. 6 are indicated with squares. Results are compared with the transport properties of axons, and myelinated axons. **c** A voltage pulse simulating an action potential (blue) is recorded at different sites along a PEDOT:PSS channel with length 1200 µm. Data show the effect of attenuation and dispersion of the traveling signal. **d** Normalized transconductance g_m^* and propagation constant γ^* of known OMIEC formulations. Both parameters must be considered to benchmark organic mixed conductors for specific applications.

length ($L \to \infty$). For short channels, information on the signal attenuation and dispersion can be obtained from Eq.2, but both the amplitude and phase of the travelling potential wave lack explicit analytical expressions as more complicated boundary conditions become relevant. However, given the overall good agreement between measurement results in Fig. 5a, b and the transmission line model predictions, we believe that the infinite line model is a reasonable approximation for our system providing reliable quantitative predictions for signal propagation in the OMIEC channel. Within this approximation, Eq. 7 demonstrates that at lower frequencies the signal attenuation and speed are fully determined by the electronic conductivity and the volumetric capacitance of the mixed conducting channel. Importantly, parameters describing the channel geometry such as channel width or thickness are no longer of relevance in this regime. At the same time, OMIEC channels should be designed with a length shorter than the characteristic value $\lambda_{LF} = \frac{1}{\alpha_{LF}} = \sqrt{\frac{2\sigma_{el}}{\omega c_v}}$ (see Eq. S27 in Supp. Inf. 6) to avoid significative signal attenuation. We note that the lower frequency regime is particularly relevant for applications of OMIECs in bioelectronics, where typical signal frequencies are below 1 kHz. On the other hand, at higher frequency the phase velocity of the propagating wave largely increases, but the attenuation coefficient plateaus at a maximum value. The limiting expression for this regime is derived in Supp. Inf. 6 and shows that the ionic conductivity in the vertical direction as well as the channel geometry become decisive. High frequency signals travelling in thicker OMIEC channels experience less attenuation and increased phase velocity.

These findings provide the means to quantitatively compare the charge transport properties of PEDOT:PSS channels with those of neural axons, addressing the analogy presented in Fig. 2. Results are reported in Fig. 5a, b. Literature values (see Supp. Inf. 7) are used to calculate signal velocity and attenuation along axons[31]. Data traces demonstrate that attenuation in PEDOT:PSS channels is significantly larger than in axons, and the signal velocity is substantially lower. This is attributed to the strong capacitive coupling between PEDOT:PSS and the electrolyte, caused by the large volumetric capacitance typical of OMIEC materials. The attenuation and signal velocity trends for myelinated axons clearly show that reducing capacitive coupling with the surrounding conductive medium mitigates attenuation, thereby enhancing signal transmission speed. These considerations are valid for single-harmonic potential waves and can be easily extended to more complex biological signals. Each Fourier component of the propagating wave package experiences attenuation and phase shift while travelling in a dissipative system. As an example, Fig. 5c illustrates the propagation of an action potential-like pulse along a 1200 μm PEDOT:PSS channel as measured in our experiments. The applied signal (blue line in Fig. 5c) contains an initial fast rise in voltage, simulating membrane depolarization, and then quickly drops into to negative voltages, representing the cell refractory period, before stabilizing back at the resting value. Measurements of the electrical signal at different positions along the channel demonstrate that due to dissipation, the signal loses in amplitude, delays in time and is also distorted in shape. For example, the information on the refractory period is completely lost at 600 μm from the injecting contact (red line in Fig. 5c).

In conclusion, we propose that our findings on dissipative transport along mixed-conducting channels hold two major implications for advancing OMIEC materials science. First, the interpretation of signal propagation spectroscopies with the transmission line theory provides a new tool to accurately measure the volumetric capacitance, electronic conductivity and ionic conductivity of organic mixed conductors during operation. This method accounts for transport in different spatial directions and multiple frequencies as relevant for transport along OMIEC channels in contact with an electrolyte bath. Second, the evidence of dissipative charge transport in OMIEC channels introduces a new paradigm for material design. Findings discussed in Fig. 5a, b indicate that OMIEC materials should be designed with low volumetric capacitance to reduce the attenuation and increase the speed of propagating signals. In current research, the universally recognized figure of merit to benchmark organic mixed conductors is given by the product of the electronic mobility and the volumetric capacitance and $\mu_{el}{}^{*}c_v$[36]. This quantity arises from the definition of transconductance for organic electrochemical transistors (OECTs), which defines the amplification properties of the transistor[4]. Transconductance is directly proportional to $\mu_{el}{}^{*}c_v$, indicating that higher electronic mobility and volumetric capacitance enhance the amplification properties of the channel. However, our work demonstrates that this description, while correct, is incomplete. High volumetric capacitance leads to increased signal dissipation, compromising transmission along the OMIEC channel. In the frequency range of biological signals (<1 kHz), the propagation constant for mixed conductors can be approximated with the low frequency limit (Eq. 7). Considering the electronic conductivity $\sigma_{el} = pe\mu_{el}$ (where p is the hole (electron) density and e the elementary charge), we can introduce the reduced propagation constant $\gamma^{*} = \sqrt{\frac{c_v}{\mu}}$ as novel figure of merit for the material charge dissipation properties. Figure 5d compares γ^{*} and the transconductance per unit area and applied voltage $g_m{}^{*} = \mu{}^{*}c_v$ for five well-known OMIEC formulations[36]. Both parameters must be considered to benchmark mixed organic conductors for specific applications. Large $g_m{}^{*}$ values are highly wanted to improve the amplification properties of biosensors, but at the same time the propagation constant must be minimized to reduce power dissipation when AC signals are transmitted. Our analysis clearly indicates that an optimized balance between these fundamental material parameters can only be obtained when increases in the volumetric capacitance of mixed conductors are combined with an increase in the electronic carrier mobility.

Methods

Device fabrication

Glass substrates (50×25 mm^2) were cleaned by sonication in acetone/isopropanol/distilled water baths. After a dehydration step (10 minutes at 110 °C), the Microposit S1818 positive photoresist was spin coated (4000 rpm for 60 s) and annealed at 110 °C for 1 minute. Metallic contacts were patterned through direct writing lithography by using the ML3 Microwriter (from Durham Magneto Optics). The photoresist was developed with Microposit MF-319 developer. Then, 7 nm of chromium and 30 nm of gold were deposited by thermal evaporation. Samples were immersed in acetone for 4 hours for photoresist lift-off. Metallic contacts were encapsulated with the mr-DWL 5 negative photoresist (from Micro Resist Technology). The resin was spin coated at 3000 rpm for 30 s and annealed at 100 °C for 2 minutes. After laser exposure, samples were baked at 100 °C for 2 minutes and relaxed for 1 hour at room temperature. Development was performed with mr-Dev 600 developer (Micro Resist Technology), and the resist was finally hard-baked at 120 °C for 30 minutes. A layer of S1818 was spin-coated (2000 rpm for 60 s) for the photolithography of the PEDOT:PSS channel. After development, substrates were treated with air plasma (15 W for 4 min) and the PEDOT:PSS solution (94% PEDOT:PSS (Heraeus, Clevios PH1000), 5% of ethylene glycol (EG) (Sigma Aldrich), 1% of 3-glycidoxypropyltrimethoxysilane (GOPS), and 0.25% of 4-dodecylbenzenesulfonicacid (DBSA)) was spin coated at 3000 rpm for 9 s. The resulting film thickness was (180 ± 10) nm. The samples were subsequently annealed at 120 °C for 1 h, and S1818 was finally lifted-off after 4 hours in isopropanol.

Electrical measurements

The electrochemical characterization of the multielectrode PEDOT:PSS channels (see Fig. 3a) was performed in liquid, using 0.1 M PBS

as electrolyte and an Ag/AgCl wire as reference electrode. AC measurements were performed with the MFLI lock-in amplifier (from Zurich Instruments). A sinusoidal oscillation V_{in} (amplitude of 10 mV) with desired frequency f was applied to the OMIEC film (vs Ag/AgCl) from the first gold microelectrode composing the multielectrode structure. A DC offset was superimposed on V_{in} to introduce an electrochemical potential E and control the conductivity of PEDOT:PSS through electrochemical doping/de-doping. The electrical potential V measured at each electrode and the dissipated AC current flowing in the electrolyte were demodulated to measure the amplitude and phase shift with respect to the applied AC voltage V_{in}. Spectroscopy experiments were performed by sweeping the frequency of V_{in} from 10 Hz to 100 kHz.

mEC-AFM imaging experiments

Atomic force microscopy (Park System's NX10 AFM) was performed in liquid, using 0.1 M PBS as electrolyte and an Ag/AgCl wire as reference electrode. A sinusoidal oscillation V_{in} (amplitude of 10 mV) with desired frequency f was applied to the OMIEC film (vs Ag/AgCl) from the first gold microelectrode composing the multielectrode structure. A DC offset was superimposed on V_{in} to introduce an electrochemical potential E and control the conductivity of PEDOT:PSS through electrochemical doping/de-doping. The cantilever sensitivity $s_c = 119 \pm 1$ V/μm of NSC36 probes was measured through repeated force-distance spectroscopies on the glass substrate of the samples (see ref. 32 for full experimental details). Multichannel images were obtained on a PEDOT:PSS layer with width $W = 50$ μm and length $L = 1.2$ mm by operating the Park NX10 AFM in PinPoint mode. The basic operation parameters were set as follows: cantilever approach/retract speed = 10 μm s^{-1}, force set point = 15.9 nN, z-servo duration = 5 ms, average time = 1.8 ms, pixel-to-pixel move time = 3 ms. In parallel, we measured the amplitude and phase of the electroswelling signal (defined as the ratio between the cantilever deflection and its sensitivity) and sent them as input to the AFM software to determine their mean value during the average time. The frequency of the input voltage V_{in} was kept constant to 1.1 kHz. mEC-AFM images were acquired on a specific area of the PEDOT:PSS layer (128x32 pixels on a 50x12.5 μm scan area) close to the injecting contact at two different electrochemical potentials ($E = 0$ V, $E = -0.2$ V). The z-scanner motion range was restricted to 3 μm.

Data availability

The data supporting the findings of this study are available within the article and its Supplementary Information. Source data are provided with this paper.

References

1. Ferro, M. D. & Melosh, N. A. Electronic and ionic materials for neurointerfaces. *Adv. Funct. Mater.* **28**, 1704335 (2018).
2. Owens, R. M. & Malliaras, G. G. Organic electronics at the interface with biology. *MRS Bull* **35**, 449–456 (2010).
3. Rivnay, J., Owens, R. M. & Malliaras, G. G. The rise of organic bioelectronics. *Chem. Mater.* **26**, 679–685 (2014).
4. Bonafè, F. et al. AC amplification gain in organic electrochemical transistors for impedance-based single cell sensors. *Nat. Commun.* **13**, 1–9 (2022).
5. Bianchi, M. et al. Poly(3,4-ethylenedioxythiophene)-based neural interfaces for recording and stimulation: fundamental aspects and in vivo applications. *Adv. Sci.* **9**, 2104701 (2022).
6. Zhang, C. et al. Organic mixed ionic electronic conductor nanochannels for vertical electrochemical and ionic transistors. *Adv. Electron. Mater.* **10**, 2300762 (2024).
7. Krauhausen, I., Coen, C.-T., Spolaor, S., Gkoupidenis, P. & van de Burgt, Y. Brain-inspired organic electronics: merging neuromorphic computing and bioelectronics using conductive polymers. *Adv. Funct. Mater.* **34**, 2307729 (2024).
8. Dominguez-Alfaro, A. et al. Light-based 3D multi-material printing of micro-structured bio-shaped, conducting and dry adhesive electrodes for bioelectronics. *Adv. Sci.* **11**, 2306424 (2024).
9. Li, C. et al. Engineering Conductive Hydrogels with Tissue-like Properties: A 3D Bioprinting and Enzymatic Polymerization Approach. *Small Sci.* **4**, 2400290 (2024).
10. Paul, C. R. *Fundamentals of Electric Circuit Analysis*. (John Wiley & Sons, 2001).
11. Hayt, W. H. *Engineering Electromagnetics*. (McGraw-Hill, 1989).
12. Bonafè, F., Decataldo, F., Fraboni, B. & Cramer, T. Charge carrier mobility in organic mixed ionic–electronic conductors by the electrolyte-gated van der Pauw Method. *Adv. Electron. Mater.* 2100086 https://doi.org/10.1002/aelm.202100086.(2021)
13. Paulsen, B. D., Tybrandt, K., Stavrinidou, E. & Rivnay, J. Organic mixed ionic–electronic conductors. *Nat. Mater.* **19**, 13–26 (2020).
14. Hodgkin, A. L. & Huxley, A. F. A quantitative description of membrane current and its application to conduction and excitation in nerve. *J. Physiol.* **117**, 500–544 (1952).
15. Wang, X., Shapiro, B. & Smela, E. Development of a model for charge transport in conjugated polymers. *J. Phys. Chem. C* **113**, 382–401 (2009).
16. Tybrandt, K., Zozoulenko, I. V. & Berggren, M. Chemical potential-electric double layer coupling in conjugated polymer-polyelectrolyte blends. *Sci. Adv.* **3**, 1–8 (2017).
17. Keene, S. T., Rao, A. & Malliaras, G. G. The relationship between ionic-electronic coupling and transport in organic mixed conductors. *Sci. Adv.* **9**, eadi3536 (2023).
18. Kaphle, V., Paudel, P. R., Dahal, D., Radha Krishnan, R. K. & Lüssem, B. Finding the equilibrium of organic electrochemical transistors. *Nat. Commun.* https://doi.org/10.1038/s41467-020-16252-2 (2020).
19. Bisquert, J., Ilyassov, B. & Tessler, N. Switching response in organic electrochemical transistors by ionic diffusion and electronic transport. *Adv. Sci.* **11**, 2404182 (2024).
20. Cucchi, M. et al. Thermodynamics of organic electrochemical transistors. *Nat. Commun.* **13**, 4514 (2022).
21. Zanotti, R. et al. Charge carrier density in organic semiconductors modulates the effective capacitance: a unified view of electrolyte gated organic transistors. *Adv. Mater.* **36**, 2410940 (2024).
22. Volkov, A. V. et al. Understanding the capacitance of PEDOT:PSS. *Adv. Funct. Mater.* **27**, 1700329 (2017).
23. Proctor, C. M., Rivnay, J. & Malliaras, G. G. Understanding volumetric capacitance in conducting polymers. *J. Polym. Sci. Part B Polym. Phys.* **54**, 1433–1436 (2016).
24. Jamnik, J. & Maier, J. Generalised equivalent circuits for mass and charge transport: chemical capacitance and its implications. *Phys. Chem. Chem. Phys.* **3**, 1668–1678 (2001).
25. Rubinson, J. F. & Kayinamura, Y. P. Charge transport in conducting polymers: insights from impedance spectroscopy. *Chem. Soc. Rev.* **38**, 3339–3347 (2009).
26. Bonafè, F., Dong, C., Malliaras, G. G., Cramer, T. & Fraboni, B. Subsurface profiling of ion migration and swelling in conducting polymer actuators with modulated electrochemical atomic force microscopy. *ACS Appl. Mater. Interfaces* **16**, 36727–36734 (2024).
27. Paulsen, B. D., Fabiano, S. & Rivnay, J. Mixed ionic-electronic transport in polymers. *Annu. Rev. Mater. Res.* **51**, 73–99 (2021).
28. de Levie, R. On porous electrodes in electrolyte solutions: I. Capacitance effects. *Electrochimica Acta* **8**, 751–780 (1963).
29. Baruah, S. M. B., Gogoi, P. & Roy, S. From Cable Equation to Active and Passive Nerve Membrane Model. in *2019 Second International Conference on Advanced Computational and Communication Paradigms (ICACCP)* 1–5. https://doi.org/10.1109/ICACCP.2019.8883011 (2019)
30. Tuckwell, H. C. *Introduction to Theoretical Neurobiology: Linear Cable Theory and Dendritic Structure*. (Cambridge University Press, 1988).

31. Nelson, P. C. & Nelson, P. *Biological Physics*. (WH Freeman New York, 2004).
32. Bonafè, F., Decataldo, F., Cramer, T. & Fraboni, B. Ionic solvent shell drives electroactuation in organic mixed ionic-electronic conductors. *Adv. Sci.* **11**, 2308746 (2024).
33. Stavrinidou, E. et al. Direct measurement of ion mobility in a conducting polymer. *Adv. Mater.* **25**, 4488–4493 (2013).
34. Li, G. & Pickup, P. G. Ion transport in poly(3,4-ethylenedioxythiophene)–poly(styrene-4-sulfonate) composites. *Phys. Chem. Chem. Phys.* **2**, 1255–1260 (2000).
35. Fan, Z., Du, D., Yao, H. & Ouyang, J. Higher PEDOT molecular weight giving rise to higher thermoelectric property of PEDOT:PSS: A comparative study of clevios P and Clevios PH1000. *ACS Appl. Mater. Interfaces* **9**, 11732–11738 (2017).
36. Inal, S., Malliaras, G. G. & Rivnay, J. Benchmarking organic mixed conductors for transistors. *Nat. Commun.* **8**, 1767 (2017).

Acknowledgements

The research leading to these results has received funding from the European Union - NextGenerationEU through the Italian Ministry of University and Research under PNRR - M4C2-I1.3 Project PE_00000019 "HEALITALIA" to Tobias Cramer CUP J32G19001080005. BF acknowledges funding by the project "Wound hEAling Real time monitoring Multisensing Electronics (WEAR-ME!)" supported by the Italian Space Agency (ASI), Contract ASI n. 2023-3-U.0, Project CUP J23C23000100005.

Author contributions

F.B. and M.B. contributed equally to this work. T.C. conceived the experiments. F.B. fabricated the PEDOT:PSS microstructured channels and performed the mEC-AFM experiments. M.B performed the electrical measurements and developed the mathematical model. F.B., M.B. and T.C. wrote the manuscript with input from all other coauthors. B.F. supervised the project.

Competing interests

The authors declare no competing interests.

Additional information

Supplementary information The online version contains supplementary material available at https://doi.org/10.1038/s41467-025-57528-9.

Correspondence and requests for materials should be addressed to Tobias Cramer.

Peer review information *Nature Communications* thanks the anonymous reviewers for their contribution to the peer review of this work. A peer review file is available.